A multi-scale control-volume finite element method for advection-diffusion equations.

Pavel Bochev[1,*], Kara Peterson, Mauro Perego

Computational Mathematics, MS1320, Sandia National Laboratories, P.O. Box 5800, Albuquerque, New Mexico 87185

Abstract

We present a new multi-scale stabilized method for advection-diffusion equations, which combines a Control Volume Finite Element (CVFEM) formulation of the governing equations with a novel multi-scale approximation of the total flux. To define the latter we solve the governing equations along suitable mesh segments under the assumption that the flux varies linearly along these segments. This procedure yields second-order accurate fluxes on the edges of the mesh. Then we use curl-conforming elements of the same order to lift these edge fluxes into the mesh elements. In so doing we obtain a stabilized CVFEM formulation that is second-order accurate and does not require mesh-dependent stabilization parameters. Several standard advection tests illustrate the computational properties of the new method.

Keywords: Advection-diffusion, Control Volume Finite Element Method, multi-scale flux, edge elements, Scharfetter-Gummel upwinding.

1. Introduction

We consider the numerical solution of the scalar advection-diffusion equation

$$\begin{cases} -\nabla \cdot F(\phi) = f & \text{in } \Omega \\ F(\phi) = (\varepsilon \nabla \phi - \mathbf{u}\phi) & \text{in } \Omega \\ \phi = g & \text{on } \Gamma \end{cases} \tag{1}$$

where $\Omega \subset \Re^n$, $n = 2, 3$ is a bounded domain with Lipschitz-continuous boundary $\Gamma = \partial\Omega$, ε is a diffusion coefficient, $\mathbf{u}$ is advective velocity, f is a given right hand side and g is a given boundary data. For brevity we restrict attention to Dirichlet boundary conditions. Extension of the approach to Neumann and mixed Neumann-Dirichlet boundary conditions is straightforward.

When $f = 0$, the first equation in (1) implies that the total flux through the boundary of an arbitrary volume in Ω equals zero. Accurate and physically consistent numerical solution of (1)

*Corresponding author

Email addresses: pbboche@sandia.gov (Pavel Bochev), kjpeter@sandia.gov (Kara Peterson), mperego@sandia.gov (Mauro Perego)

URL: http://www.cs.sandia.gov/~pbboche/ (Pavel Bochev)

[1]Sandia National Laboratories is a multi-program laboratory managed and operated by Sandia Corporation, a wholly owned subsidiary of Lockheed Martin Corporation, for the U.S. Department of Energy's National Nuclear Security Administration under contract DE-AC04-94AL85000.

requires numerical methods that preserve some notion of this *local conservation* property. In addition, these methods should remain stable in the advection-dominated regime, i.e., when ε is small relative to $\mathbf{u}$. This regime may lead to the appearance of internal and/or boundary layers in the solution of (1). If the grid is not fine enough to resolve these layers, numerical solutions can develop spurious oscillations [17].

In this paper we present a new parameter-free stabilized method for (1), which combines a Control Volume Finite Element (CVFEM) formulation [3] of the governing equations with a novel multi-scale approximation of the flux $F(\phi)$. We choose CVFEM as a foundation for our method because it combines the straightforward nodal reconstruction of Galerkin methods with the local conservation properties of finite volume schemes. However, our CVFEM stabilization strategy differs substantially from published approaches [25, 24], which use the same perturbation functions as the Streamline Upwind Petrov-Galerkin (SUPG) method [7, 15].

Resulting Streamline Upwind Control Volume (SUCV) methods are first-order accurate and inherit the mesh-dependent SUPG stabilization parameter τ. The choice of this parameter is critical for the accuracy and stability of the approximate numerical solution. Yet, because this parameter depends on mesh constants that are known only in special cases [13], and because different solution features generally require different definitions of this parameter, finding the best possible τ for a given problem remains an open question [18, 8].

In contrast, we stabilize CVFEM through a multi-scale flux approximation, which does not involve tunable mesh-dependent parameters and is defined by an $H(curl)$ lifting of one-dimensional edge fluxes into the elements. This stabilization strategy originated in [6] where we combined a classical Scharfetter-Gummel upwinding to define first-order accurate fluxes on mesh edges with the lowest-order curl-conforming Nedelec space [20, 21] to expand these fluxes into the elements. In so doing we obtained a parameter-free first-order accurate *exponentially-fitted* CVFEM[2] for (1).

The principal goal of this paper is to develop further the $H(curl)$ stabilization approach and demonstrate its potential by extending it to a second-order accurate CVFEM formulation. Succinctly, we consider $H(curl)$ lifting of second-order accurate edge fluxes by a curl-conforming edge element space of the same order. Since construction of the latter is well-understood for a wide range of elements shapes [20, 21, 9, 2], a key juncture towards our goal is the definition of second-order edge fluxes that match the vectorial degrees-of-freedom. To this end, we solve one-dimensional versions of the governing equations on suitable line segments. Specifically, given a line segment $\boldsymbol{s}$ containing a pair of of vectorial degrees-of-freedom we construct a matching pair of one-dimensional fluxes as follows. First, we restrict (1) to the segment and find its general solution under the assumption that F is linear along $\boldsymbol{s}$. Then we select a particular solution by requiring that the former interpolates the nodal values of ϕ along segment $\boldsymbol{s}$. Finally, we use this particular solution to compute the flux at the two halves of the segment.

This strategy can be viewed as "bootstrapping" of the classical Scharfetter-Gummel upwinding. Indeed the latter solves (1) on individual mesh edges under the assumption that $F = const$ to obtain first-order fluxes relating the values of ϕ at the endpoints of a *single edge*. In contrast, we assume that F varies linearly along segments comprising pairs of edges and solve (1) on these segments. In so doing we obtain second-order accurate edge fluxes, which relate the nodal values of ϕ on *pairs of edges*. We show that these fluxes are perturbations of the classical Scharfetter-Gummel fluxes by higher-order terms, which motivates the term "multi-scale flux" for their $H(curl)$ lifting into the elements.

[2]For a related finite element method and its analysis we refer to [5] and [4].

Broadly speaking our approach belongs in a category of numerical methods which use exact analytic solutions of simplified governing equations to improve the stability and accuracy of the numerical solutions. What sets our approach apart from published work is the manner in which the information from the analytical solution is incorporated in the numerical scheme. Typically, existing methods use analytic solutions to define enriched, multi-scale or exponentially fitted shape functions for the finite element method, see, e.g., [14, 12, 11, 26, 22, 1] for representative examples of this approach. These shape functions are then used to enrich or even completely replace standard piecewise polynomial bases in a weak finite element formulation of the problem.

In contrast, our approach does not involve enrichment or substitution of the standard nodal shape functions. Instead, we use the analytic solutions to approximate directly the flux of the exact solution by virtue of curl-conforming edge elements. In so doing we avoid the need to introduce stabilizing parameters whose purpose is to "blend" together distinct discretization spaces into a single stable approximation.

We have organized the rest of the paper as follows. Section 1.1 reviews the relevant notation and Section 2 presents the new multi-scale CVFEM. Section 3 provides a brief asymptotic analysis of the multi-scale flux approximation. Section 4 uses manufactured solutions and several standard advection test problems to illustrate numerically the quantitative and qualitative properties of the method. It also briefly describes the assembly process for the new method.

1.1. Notation

In this paper $\Omega \subset \Re^n$, $n = 2, 3$ is a bounded open region with a Lipschitz-continuous boundary Γ, $H^k(\Omega)$ is a Sobolev space of order k, $H^k_0(\Omega)$ is the subspace of functions in $H^k(\Omega)$ whose traces vanish on Γ, $L^2(\Omega) = H^0(\Omega)$, and $H(curl, \Omega)$ is the space of all vector fields in $L^2(\Omega)^n$ whose curl belongs in $L^2(\Omega)^{2n-3}$.

Finite element partition. For clarity we formulate the new multi-scale stabilized CVFEM in two-dimensions using a conforming partition $K_h(\Omega)$ of Ω into quadrilateral elements K_s. Appendix B briefly discusses extensions to three-dimensions. The medians of an element $K_s \in K_h(\Omega)$ subdivide it into four quadrilateral sub-elements K_{s_i}, $i = 1, \ldots, 4$. The set of all sub-elements forms another conforming partition $\widetilde{K}_h(\Omega)$ of Ω into quadrilateral elements. The set of all vertices in the sub-element partition coincides with the union of all vertices, centers and side midpoints of the elements in $K_h(\Omega)$; see Fig. 1(a). We refer to this set as the *set of all mesh points* $\{\boldsymbol{p}_i\}$. Every two adjacent points $\boldsymbol{p}_i$ and $\boldsymbol{p}_j$ on an element side or a median define a *sub-edge* $\boldsymbol{e}_{ij}$; see Fig. 1 (b). Two collinear sub-edges $\boldsymbol{e}_{ij}$ and $\boldsymbol{e}_{jk}$, sharing a point $\boldsymbol{p}_j$ form a *segment* $\boldsymbol{s}_{ijk}$ with vertices $\boldsymbol{p}_i$ and $\boldsymbol{p}_k$; see Fig. 1 (c). We orient a segment $\boldsymbol{s}_{ijk}$ by choosing the order of $\boldsymbol{p}_i$ and $\boldsymbol{p}_k$. The sub-edges $\boldsymbol{e}_{ij}$ and $\boldsymbol{e}_{jk}$ comprising the segment inherit its orientation. For instance, if $\boldsymbol{p}_i$ is the first vertex of $\boldsymbol{s}_{ijk}$ and $\boldsymbol{p}_k$ is its second vertex, then $\boldsymbol{p}_i$ is the first vertex of $\boldsymbol{e}_{ij}$ and $\boldsymbol{p}_k$ is the second vertex of $\boldsymbol{e}_{jk}$

For clarity, whenever appropriate we also use the more compact notation $\boldsymbol{e}_\alpha$ and $\boldsymbol{s}_\beta$, where α and β are multi-indices containing the numbers of the endpoints of $\boldsymbol{e}_\alpha$, and the endpoints and the midpoint of $\boldsymbol{s}_\beta$, respectively.

We denote the sets of points, sub-edges, segments, and elements on $K_h(\Omega)$, intersecting with an entity $\omega \subset \overline{\Omega}$, by $P(\omega)$, $E(\omega)$, $S(\omega)$ and $K(\omega)$, respectively. For instance, $P(\Omega)$ is the set of all interior points in $K_h(\Omega)$, $E(K_{s_i})$ are the sub-edges belonging to a sub-element $K_{s_i} \subset K_s$, and $S(K_s)$ is the set of all segments in K_s. The set $\widetilde{K}(\omega)$ contains all sub-elements intersecting ω.

Given a point $\boldsymbol{p}_j \in P(\Omega)$ we define the associated control volume C_j by connecting the barycenter of every sub-element $K_{s_i} \in \widetilde{K}(\boldsymbol{p}_j)$ with the midpoints of the two sub-edges in $E(\boldsymbol{p}_j) \cap E(K_{s_i})$; see Fig. 2. If $K_h(\Omega)$ is rectilinear, then the set of all control volumes forms a

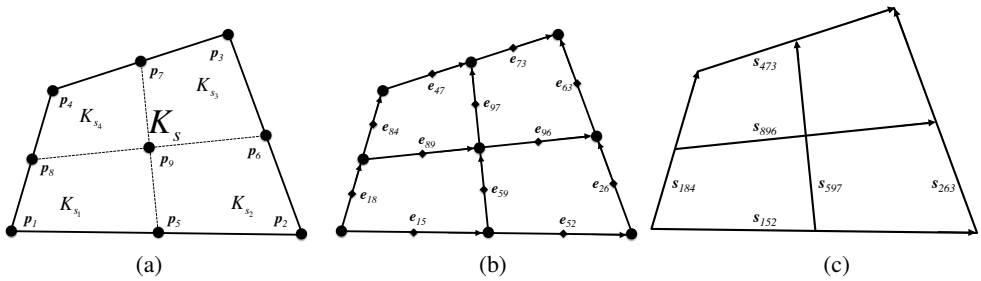

Figure 1: Mesh nomenclature: (a) a finite element $K_s \in K_h(\Omega)$, its sub-elements and its points ; (b) element sub-edges and vectorial finite element degrees-of-freedom (diamonds); (c) element segments

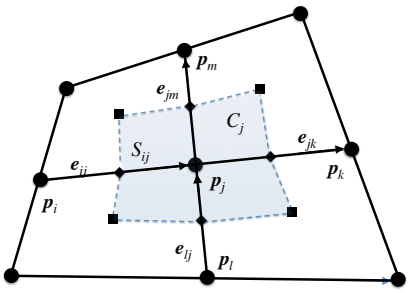

Figure 2: Connecting the barycenter of every sub-element $K_{s_i} \in \widetilde{K}(\boldsymbol{p}_j)$ (squares) with the midpoints of the two sub-edges in $E(\boldsymbol{p}_j) \cap E(K_{s_i})$ (diamonds) defines a *median bisector* control volume associated with mesh point $\boldsymbol{p}_j$.

topologically dual rectilinear mesh partition. In this case, the sides of the control volumes are dual to the sub-edges on the primal grid $K_h(\Omega)$. In general though, the boundary of C_j is a polygon with $2 \times |E(\boldsymbol{p}_j)|$ sides; see Fig. 2. We denote the union of the two sides connected to the midpoint of sub-edge $\boldsymbol{e}_{ij}$ by S_{ij}. Thus,

$$\partial C_j = \bigcup_{\boldsymbol{e}_{ij} \in E(\boldsymbol{p}_j)} S_{ij}$$

For instance, if $K_h(\Omega)$ is logically Cartesian then the control volumes associated with interior mesh points are octagons.

Finite element spaces. To construct a multi-scale approximation of the flux $F(\phi)$ in Section 2.2 we first define second-order accurate fluxes on element sub-edges and then expand them into the elements by using curl-conforming finite element spaces. Consequently, the number of edge element degrees-of-freedom per element must match the number of element's sub-edges. A quadrilateral has 12 sub-edges and so, the appropriate space to perform the lifting of the edge fluxes in this case is the second-order Nedelec edge element space of the first kind [20]. We denote this space by $E_h(\Omega)$ and $\{\vec{W}_\alpha\}$ is the corresponding set of basis functions, indexed by a sub-edge. For the purposes of this paper it is convenient to work with basis functions having the

property that[3]

$$\vec{W}_\alpha \cdot \boldsymbol{t}_\beta \Big|_{\boldsymbol{m}_\beta} = \delta_\alpha^\beta \qquad \forall \boldsymbol{e}_\beta, \boldsymbol{e}_\alpha \in E(\Omega)\,, \tag{2}$$

where $\boldsymbol{m}_\beta$ is the midpoint of sub-edge $\boldsymbol{e}_\beta$.

For the approximation of ϕ we can use any finite element space that is second or higher order accurate, and whose degrees-of-freedom are located at the mesh points $\{\boldsymbol{p}_i\}$. Two obvious choices are a standard C^0 biquadratic space defined with respect to $K_h(\Omega)$ and a standard C^0 bilinear space defined with respect to the sub-element mesh $\widetilde{K}_h(\Omega)$.

Both spaces have the same number of degrees-of-freedom and lead to algebraic problems of the same size. The first choice could be useful if one does not wish to establish a data structure for the sub-element mesh $\widetilde{K}_h(\Omega)$, but it would not take full advantage of the third-order accuracy of the biquadratic element. The bilinear finite element matches the accuracy of the multi-scale flux approximation and so we choose to state the method using this space. Thus, in what follows $\widetilde{N}_h(\Omega)$ is the standard C^0 bilinear nodal space defined with respect to the *sub-element* mesh $\widetilde{K}_h(\Omega)$, $\widetilde{N}_{h,0}(\Omega)$ is the subspace of $\widetilde{N}_h(\Omega)$ containing functions that vanish on Γ, and $\{\widetilde{N}_i\}_{\boldsymbol{p}_i \in P(\overline{\Omega})}$ is the standard Lagrangian nodal basis, i.e., $\widetilde{N}_i(\boldsymbol{x}_i)$ are C^0, piecewise bilinear functions such that

$$\widetilde{N}_i(\boldsymbol{p}_j) = \delta_i^j\,.$$

We denote the coefficient vector of a finite element function $\phi_h \in \widetilde{N}_h(\Omega)$ by $\boldsymbol{\phi} = (\phi_1, \ldots, \phi_p)$ where $p = |P(\overline{\Omega})|$ is the number of all points in the mesh.

2. Stabilized multi-scale CVFEM

The new parameter-free stabilized CVFEM combines a CVFEM approach [3] with a new multi-scale approximation of the total flux $F(\phi)$. In §2.1 we use the CVFEM framework to derive a general formulation of our method. Section 2.2 explains the construction of the multi-scale flux approximation.

2.1. A general CVFEM formulation of the model problem

For simplicity we restrict attention to formulations which impose the Dirichlet boundary conditions strongly, i.e., we seek finite element solutions of (1) in the form

$$\phi_h(\boldsymbol{x}) = \sum_{\boldsymbol{p}_i \in P(\Omega)} \phi_i \widetilde{N}_i(\boldsymbol{x}) + \sum_{\boldsymbol{p}_j \in P(\Gamma)} g(\boldsymbol{p}_j) \widetilde{N}_j(\boldsymbol{x})\,. \tag{3}$$

This form corresponds to a partition $\boldsymbol{\phi} = (\boldsymbol{\phi}_0, \boldsymbol{\phi}_g)$ of the finite element degrees of freedom into a vector of unknown nodal coefficients $\boldsymbol{\phi}_0$ with dimension $p_0 = |P(\Omega)|$, associated with the interior points $\boldsymbol{p}_i \in P(\Omega)$, and a vector of nodal boundary values $\boldsymbol{\phi}_g$ with dimension $p_g = |P(\Gamma)|$ containing the values of $g(\boldsymbol{x})$ at the boundary points $\boldsymbol{p}_i \in P(\Gamma)$. Succinctly, the second term is the finite element interpolant $\mathcal{I}g$ of the given boundary data, whereas the first term defines a finite element function $\phi_{h,0} \in \widetilde{N}_{h,0}(\Omega)$.

With strongly imposed Dirichlet boundary conditions a CVFEM formulation for (1) involves only the control volumes associated with the interior points[4] of $K_h(\Omega)$; see Fig. 3. Accordingly,

[3] Appendix A provides detailed definitions of the edge basis functions.

[4] In the general case of mixed boundary conditions the dual mesh also includes control volumes associated with the points on the Neumann part of the boundary.

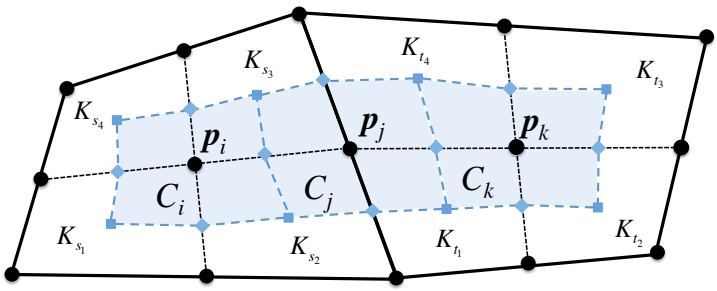

Figure 3: Quadrilateral grid $K_h(\Omega)$ comprising two elements K_s and K_t gives rise to a sub-element grid $\widetilde{K}_h(\Omega)$ with 8 sub-elements. The control volumes C_i, C_j and C_k are associated with the interior points $P(\Omega) = \{\boldsymbol{p}_i, \boldsymbol{p}_j, \boldsymbol{p}_k\}$ of $K_h(\Omega)$. The volumes C_i and C_k are entirely contained in the interiors of K_s and K_t, respectively, whereas C_j intersects these two elements.

to obtain the "weak" CVFEM form of (1) one integrates the first equation in (1) on these control volumes and then applies the Divergence Theorem to obtain the following system of $n_0 = |P(\Omega)|$ "weak" equations:

$$\int_{\partial C_i} F(\phi) \cdot \boldsymbol{n}\, dS = \int_{C_i} f dV \qquad \forall \boldsymbol{p}_i \in P(\Omega)\,. \tag{4}$$

Transformation of volume integrals into surface integrals reduces the order of differentiation from two to one and so, the "weak" equations (4) are well-defined for finite element functions in $N_h(\Omega)$. Restriction of (4) to $\widetilde{N}_h(\Omega)$ then yields a standard nodal CVFEM on the sub-element grid $\widetilde{K}_h(\Omega)$: seek a finite element function $\phi_h \in \widetilde{N}_h(\Omega)$, given by (3), such that

$$\int_{\partial C_i} F(\phi_h) \cdot \boldsymbol{n}\, dS = \int_{C_i} f dV \qquad \forall \boldsymbol{p}_i \in P(\Omega)\,. \tag{5}$$

It is easy to see that (5) is a $p_0 \times p_0$ system of linear algebraic equations $A\boldsymbol{\phi}_0 = \boldsymbol{f}$ for the unknown coefficient vector $\boldsymbol{\phi}_0$, where

$$A_{ij} = \int_{\partial C_i} F(\widetilde{N}_j) \cdot \boldsymbol{n}\, dS \quad \text{and} \quad \boldsymbol{f}_i = \int_{C_i} f dV - \int_{\partial C_i} F(\mathcal{I}g) \cdot \boldsymbol{n}\, dS\,. \tag{6}$$

Similar to Galerkin methods for (1) in the advection-dominated regime solutions of (5) may become unstable and develop spurious oscillations. These oscillations are brought about by the fact that when the mesh does not resolve solution layers the nodal approximation of the total flux

$$F(\phi_h) = \varepsilon \nabla \phi_h - \mathbf{u}\phi_h = \sum_{\boldsymbol{p}_j \in P(\Omega)} \phi_j \left(\varepsilon \nabla \widetilde{N}_j(\boldsymbol{x}) - \mathbf{u}\widetilde{N}_j(\boldsymbol{x}) \right) \tag{7}$$

is not an accurate representation of the advection of ϕ between neighboring nodes [23].

In this paper we propose to stabilize (5) by replacing the nodal flux $F(\phi_h)$ with an $H(curl)$-conforming multi-scale approximation

$$F_h(\boldsymbol{\phi}) = \sum_{\boldsymbol{e}_\xi \in E(\Omega)} F_\xi(\boldsymbol{\phi}) \vec{W}_\xi\,, \tag{8}$$

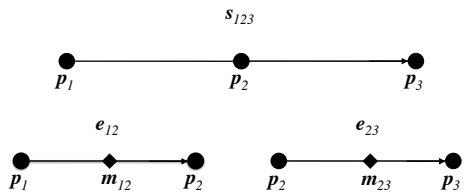

Figure 4: A segment $\boldsymbol{s}_{123}$, its points $\boldsymbol{p}_1$, $\boldsymbol{p}_2$ and $\boldsymbol{p}_3$, its sub-edges $\boldsymbol{e}_{12}$ and $\boldsymbol{e}_{23}$, and their midpoints $\boldsymbol{m}_{12}$ and $\boldsymbol{m}_{23}$.

where $F_\xi(\boldsymbol{\phi})$ are second-order fluxes specified at the midpoints $\boldsymbol{m}_\xi$ of the element sub-edges and $\vec{W}_\xi$ are the Nedelec basis functions (2). We note that, although (8) defines a global $H(curl)$-conforming field in terms of vectorial edge element basis functions, it operates on scalar unknowns associated with the mesh points rather than the mesh edges.

Using $F_h(\boldsymbol{\phi})$ in lieu of $F(\phi_h)$ yields the new multi-scale CVFEM formulation: seek ϕ_h with coefficients $\boldsymbol{\phi} = (\boldsymbol{\phi}_0, \boldsymbol{\phi}_g)$ such that

$$\int_{\partial C_i} F_h(\boldsymbol{\phi}) \cdot \boldsymbol{n}\, dS = \int_{C_i} f dV \quad \forall \boldsymbol{p}_i \in P(\Omega)\,. \tag{9}$$

This formulation is also equivalent to a $p_0 \times p_0$ system of linear algebraic equations for the unknown coefficient vector $\boldsymbol{\phi}_0$. Section 4 provides further information about the assembly of these equations.

A few comments about the multi-scale CVFEM (9) are now in order. In Section 2.2 we will derive the one-dimensional edge fluxes F_ξ using analytic solutions of the model equations along mesh segments. The resulting expressions relate the nodal values of ϕ_h along the segments without a reference to a particular nodal finite element basis. As a result, both F_ξ and the multi-scale flux F_h are *completely independent* of the choice of a nodal finite element space and act directly on the nodal degrees of freedom. To emphasize this fact we write these fluxes as functions of the vector $\boldsymbol{\phi}$ of nodal values rather than the finite element function $\phi_h(\boldsymbol{x})$.

As a consequence, the CVFEM formulation (9) does not require any notion of a nodal finite element space for ϕ and if the approximate solution is not needed in locations other than the mesh points, one can completely forego such a space.

Remark 1. *A weak CVFEM formulation of a transient version of the model problem (1) involves an additional term with the integral of the time derivative of ϕ over a control volume. Spatial discretization of such a weak form does require some means of approximating this integral. Although this can be accomplished in many different ways, the most straightforward approach is to discretize ϕ by nodal finite elements.*

2.2. Multi-scale flux approximation

We consider a single mesh segment $\boldsymbol{s}_\alpha$ with length $h_\alpha = |\boldsymbol{s}_\alpha|$ and a natural parameter s. Without loss of generality we may assume that $\alpha = (1, 2, 3)$. Accordingly, the points on this segment are $\boldsymbol{p}_1$, $\boldsymbol{p}_2$ and $\boldsymbol{p}_3$, the vector of the unknown nodal coefficients is $\boldsymbol{\phi} = (\phi_1, \phi_2, \phi_3)$, and the sub-edges comprising the segment are $\boldsymbol{e}_{12}$ and $\boldsymbol{e}_{23}$, respectively; see Fig. 4. We recall that $\boldsymbol{p}_2$ is the midpoint of $\boldsymbol{s}_\alpha$. Thus, in terms of the natural parameter $\boldsymbol{p}_1 = 0$, $\boldsymbol{p}_2 = h_\alpha/2$, $\boldsymbol{p}_3 = h_\alpha$, $\boldsymbol{m}_{12} = h_\alpha/4$, $\boldsymbol{m}_{23} = 3h_\alpha/4$, and $|\boldsymbol{e}_{12}| = |\boldsymbol{e}_{23}| = h_\alpha/2$. We assume that $\boldsymbol{s}_{123}$ is oriented by choosing $\boldsymbol{p}_1$ as its

first vertex and $\boldsymbol{p}_3$ as its second vertex. Since sub-edges inherit the orientation of their parent segment, it follows that $\boldsymbol{p}_1$ and $\boldsymbol{p}_2$ are the first vertices of $\boldsymbol{e}_{12}$ and $\boldsymbol{e}_{23}$, respectively.

The multi-scale flux approximation (8) requires second-order fluxes $F_{12}(\boldsymbol{\phi})$ and $F_{23}(\boldsymbol{\phi})$ specified at sub-edge midpoints $\boldsymbol{m}_{12}$ and $\boldsymbol{m}_{23}$, respectively. We proceed to construct these fluxes according to the following procedure. Let

$$u_\alpha = \frac{1}{h_\alpha}\int_{s_\alpha} \mathbf{u}\cdot\boldsymbol{t}_\alpha\, ds \quad \text{and} \quad \varepsilon_\alpha = \frac{1}{h_\alpha}\int_{s_\alpha} \varepsilon\, ds$$

denote the mean segment velocity and diffusion. Given a real function $\varphi : \boldsymbol{s}_\alpha \mapsto \Re$ we define its *segment flux* according to the formula

$$F_s(s) = \varepsilon_\alpha \varphi'(s) - u_\alpha \varphi(s)\,. \tag{10}$$

Assume now that $\varphi(s)$ is such that

a) $\varphi(s)$ interpolates the nodal values along the segment, i.e.,

$$\varphi(0) = \phi_1, \quad \varphi(h_\alpha/2) = \phi_2, \quad \varphi(h_\alpha) = \phi_3, \quad \text{and} \tag{11}$$

b) The segment flux of $\varphi(s)$ is a linear function, i.e.,

$$F_s(s) = A + Bs\,. \tag{12}$$

Given such a scalar function, the values of its segment flux at sub-edge midpoints define the sub-edge fluxes, i.e.,

$$F_{12}(\boldsymbol{\phi}) = F_s(h_\alpha/4) \quad \text{and} \quad F_{23}(\boldsymbol{\phi}) = F_s(3h_\alpha/4)\,. \tag{13}$$

Proposition 1. *Assume that $u_\alpha \neq 0$. Then, conditions (11)–(12) define a unique function*

$$\varphi(s) = C_1(\boldsymbol{\phi})e^{su_\alpha/\varepsilon_\alpha} + C_2(\boldsymbol{\phi}) + sC_3(\boldsymbol{\phi}) \tag{14}$$

where

$$C_1(\boldsymbol{\phi}) = \frac{\phi_1 - 2\phi_2 + \phi_3}{(e^{p_\alpha}-1)^2}; \quad C_2(\boldsymbol{\phi}) = \phi_1 - C_1; \quad C_3(\boldsymbol{\phi}) = -2\frac{e^{p_\alpha}\phi_1 - (e^{p_\alpha}+1)\phi_2 + \phi_3}{h_\alpha(e^{p_\alpha}-1)}\,, \tag{15}$$

and

$$p_\alpha = \frac{u_\alpha h_\alpha}{2\varepsilon_\alpha}$$

is the segment's Péclet number.

Proof. Assumption (12) implies that

$$F_s''(s) = \varepsilon_\alpha \varphi'''(s) - u_\alpha \varphi''(s) = 0\,.$$

It is straightforward to check that a general solution of this third-order equation is given by (14). We determine the coefficients of this solution by requiring that interpolating conditions (11) hold for $\varphi(s)$. Assuming that the mean edge velocity is not equal to zero, the resulting 3×3 linear system has a unique solution given by (15). □

Suppose now that $\varphi(s)$ is the function (14) with coefficients set according to (15). Direct calculation shows that its segment flux is the following linear function:

$$F_s(s) = -u_\alpha C_2(\boldsymbol{\phi}) + (\varepsilon_\alpha - s u_\alpha) C_3(\boldsymbol{\phi})\,.$$

We set the sub-edge fluxes according to (13), i.e.,

$$F_{12}(\boldsymbol{\phi}) = -u_\alpha C_2(\boldsymbol{\phi}) + (\varepsilon_\alpha - \frac{h_\alpha}{4} u_\alpha) C_3(\boldsymbol{\phi}) \quad \text{and} \quad F_{23}(\boldsymbol{\phi}) = -u_\alpha C_2(\boldsymbol{\phi}) + (\varepsilon_\alpha - \frac{3h_\alpha}{4} u_\alpha) C_3(\boldsymbol{\phi}). \tag{16}$$

The following proposition provides further information about the multi-scale structure of these fluxes.

Proposition 2. *The sub-edge fluxes can be written as*

$$F_{12}(\boldsymbol{\phi}) = \Phi(\phi_1, \phi_2) + \gamma(\boldsymbol{\phi}) \quad \textit{and} \quad F_{23}(\boldsymbol{\phi}) = \Phi(\phi_2, \phi_3) + \gamma(\boldsymbol{\phi}) \tag{17}$$

where

$$\Phi(\phi_{i_1}, \phi_{i_2}) = u_\alpha \left(\frac{\phi_{i_2} - e^{p_\alpha} \phi_{i_1}}{e^{p_\alpha} - 1} \right) \tag{18}$$

and

$$\gamma(\boldsymbol{\phi}) = \varepsilon_\alpha \left(1 - \frac{p_\alpha}{2} \cdot \frac{(e^{p_\alpha} + 1)}{(e^{p_\alpha} - 1)} \right) C_3(\boldsymbol{\phi})\,.$$

Proof. To prove the first identity in (17) we rewrite $C_2(\boldsymbol{\phi})$ as follows:

$$\begin{aligned}
C_2(\boldsymbol{\phi}) &= \phi_1 - \frac{\phi_1 - 2\phi_2 + \phi_3 \pm e^{p_\alpha}\phi_1 \pm e^{p_\alpha}\phi_2}{(e^{p_\alpha} - 1)^2} \\
&= \phi_1 - \frac{e^{p_\alpha}\phi_2 - e^{p_\alpha}\phi_1 - (\phi_2 - \phi_1)}{(e^{p_\alpha} - 1)^2} - \frac{e^{p_\alpha}\phi_1 - (e^{p_\alpha} + 1)\phi_2 + \phi_3}{(e^{p_\alpha} - 1)^2} \\
&= \phi_1 - \frac{\phi_2 - \phi_1}{(e^{p_\alpha} - 1)} + \frac{h_\alpha}{2(e^{p_\alpha} - 1)} \left(-2 \frac{e^{p_\alpha}\phi_1 - (e^{p_\alpha} + 1)\phi_2 + \phi_3}{h_\alpha (e^{p_\alpha} - 1)} \right) \\
&= \frac{e^{p_\alpha}\phi_1 - \phi_2}{(e^{p_\alpha} - 1)} + \frac{h_\alpha}{2(e^{p_\alpha} - 1)} C_3(\boldsymbol{\phi})\,.
\end{aligned} \tag{19}$$

Inserting the last identity into the definition of F_{12} in (16) yields the first formula in (17). To prove the second formula we start from the result in (19):

$$\begin{aligned}
C_2(\boldsymbol{\phi}) &= \frac{e^{p_\alpha}\phi_1 - \phi_2 \pm e^{p_\alpha}\phi_2 \pm \phi_3}{(e^{p_\alpha} - 1)} + \frac{h_\alpha}{2(e^{p_\alpha} - 1)} C_3(\boldsymbol{\phi}) \\
&= \frac{e^{p_\alpha}\phi_2 - \phi_3}{(e^{p_\alpha} - 1)} + \frac{e^{p_\alpha}\phi_1 - (e^{p_\alpha} + 1)\phi_2 + \phi_3}{(e^{p_\alpha} - 1)} + \frac{h_\alpha}{2(e^{p_\alpha} - 1)} C_3(\boldsymbol{\phi}) \\
&= \frac{e^{p_\alpha}\phi_2 - \phi_3}{(e^{p_\alpha} - 1)} + \frac{h_\alpha}{2} \left(\frac{1}{(e^{p_\alpha} - 1)} - 1 \right) C_3(\boldsymbol{\phi})\,.
\end{aligned}$$

Inserting the last result into the definition of F_{23} in (16) yields the second formula in (17) and completes the proof. □

This proposition reveals a connection between sub-edge fluxes F_{12} and F_{23} and classical Scharfetter-Gummel edge fluxes. Indeed, the terms

$$\Phi(\phi_1, \phi_2) = u_\alpha \left(\frac{\phi_2 - e^{p_\alpha} \phi_1}{e^{p_\alpha} - 1} \right) \quad \text{and} \quad \Phi(\phi_2, \phi_3) = u_\alpha \left(\frac{\phi_3 - e^{p_\alpha} \phi_2}{e^{p_\alpha} - 1} \right)$$

in (17) are exactly the same as one would obtain from applying the Scharfetter-Gummel formula *independently* on sub-edges $\boldsymbol{e}_{12}$ and $\boldsymbol{e}_{23}$, respectively; see e.g., [6, 5]. Succinctly, Proposition 2 states that the sub-edge fluxes are sums of *classical Scharfetter-Gummel fluxes* defined on the sub-edges, and acting only on the endpoints of these sub-edges, and a *correction term* $\gamma(\boldsymbol{\phi})$ acting on all points in the segment. This hierarchical structure of the sub-edge fluxes motivates calling them and the resulting total flux approximation (8) "multi-scale".

3. Asymptotic analysis of the multi-scale flux

This section examines the multi-scale flux approximation (8) to identify the mechanisms responsible for stabilizing the CVFEM. Assuming the same numbering and orientation as in Section 2.2 consider the restriction of $F_h(\boldsymbol{\phi})$ to a segment $\boldsymbol{s}_\alpha$

$$F_h(\boldsymbol{\phi})|_{\boldsymbol{s}_\alpha} = \sum_{\boldsymbol{e}_\xi \in E(\boldsymbol{s}_\alpha)} F_\xi(\boldsymbol{\phi}) \vec{W}_\xi|_{\boldsymbol{s}_\alpha} = F_{12}(\boldsymbol{\phi})\, \vec{W}_{12}|_{\boldsymbol{s}_\alpha} + F_{23}(\boldsymbol{\phi})\, \vec{W}_{23}|_{\boldsymbol{s}_\alpha} .$$

Without loss of generality we may assume that $\boldsymbol{t}_\alpha = \mathbf{i}$. Then, using expressions (A.2) for the "horizontal" basis functions it is not hard to see that

$$\vec{W}_{12}|_{\boldsymbol{s}_\alpha} = -\mathbf{i} \frac{2}{h_\alpha} \left(s - \frac{3h_\alpha}{4} \right) = \mathbf{i} \left(\frac{3}{2} - \frac{2s}{h_\alpha} \right) \quad \text{and} \quad \vec{W}_{23}|_{\boldsymbol{s}_\alpha} = \mathbf{i} \frac{2}{h_\alpha} \left(s - \frac{h_\alpha}{4} \right) = \mathbf{i} \left(\frac{2s}{h_\alpha} - \frac{1}{2} \right), \tag{20}$$

respectively. Consequently, restriction of the multiscale flux along a mesh segment is given by a linear function

$$F_h(\boldsymbol{\phi})|_{\boldsymbol{s}_\alpha} = \mathbf{i} \left(F_{12}(\boldsymbol{\phi}) \left(\frac{3}{2} - \frac{2s}{h_\alpha} \right) + F_{23}(\boldsymbol{\phi}) \left(\frac{2s}{h_\alpha} - \frac{1}{2} \right) \right) .$$

To analyze this function we rewrite the sub-edge fluxes and the multi-scale correction term into more convenient forms as follows. Let $q_\alpha = p_\alpha/2$. Using the identities

$$\frac{1}{e^{2a} - 1} = \frac{1}{2}(\coth a - 1) \quad \text{and} \quad \frac{e^{2a}}{e^{2a} - 1} = \frac{1}{2}(\coth a + 1)$$

the classical Scharfetter-Gummel fluxes assume the form

$$\Phi(\phi_{i_1}, \phi_{i_2}) = \frac{u_\alpha}{2} (\phi_{i_2}(\coth q_\alpha - 1) - \phi_{i_1}(\coth q_\alpha + 1))$$

for $\{i_1, i_2\} = \{1, 2\}, \{2, 3\}$, whereas the multi-scale correction term transforms to

$$\gamma(\boldsymbol{\phi}) = -\frac{\varepsilon_\alpha}{h_\alpha} (1 - q_\alpha \coth q_\alpha) (\phi_1(\coth q_\alpha + 1) - 2\phi_2 \coth q_\alpha + \phi_3(\coth q_\alpha - 1)) .$$

Note that

$$\begin{aligned}
\Phi(\phi_1,\phi_2) &= -u_\alpha\frac{\phi_1+\phi_2}{2}+\frac{u_\alpha}{2}\coth(q_\alpha)(\phi_2-\phi_1)\\
&= -u_\alpha\frac{\phi_1+\phi_2}{2}+\varepsilon_\alpha q_\alpha\coth(q_\alpha)\frac{(\phi_2-\phi_1)}{h_\alpha/2}\\
&= -u_\alpha\frac{\phi_1+\phi_2}{2}+\varepsilon_\alpha\frac{(\phi_2-\phi_1)}{h_\alpha/2}+\boxed{\varepsilon_\alpha(q_\alpha\coth(q_\alpha)-1)\frac{(\phi_2-\phi_1)}{h_\alpha/2}},
\end{aligned}$$

and analogously

$$\Phi(\phi_2,\phi_3) = -u_\alpha\frac{\phi_2+\phi_3}{2}+\varepsilon_\alpha\frac{(\phi_3-\phi_2)}{h_\alpha/2}+\boxed{\varepsilon_\alpha(q_\alpha\coth(q_\alpha)-1)\frac{(\phi_3-\phi_2)}{h_\alpha/2}}.$$

The terms

$$f_{12} := -u_\alpha\frac{\phi_1+\phi_2}{2}+\varepsilon_\alpha\frac{(\phi_2-\phi_1)}{h_\alpha/2} \quad\text{and}\quad f_{23} := -u_\alpha\frac{\phi_2+\phi_3}{2}+\varepsilon_\alpha\frac{(\phi_3-\phi_2)}{h_\alpha/2}$$

approximate solution flux at sub-edge midpoints $\boldsymbol{m}_{12}$ and $\boldsymbol{m}_{23}$, respectively, while the boxed expressions are stabilizing diffusive fluxes on the sub-edges. We also have that

$$\gamma(\boldsymbol{\phi}) = -\varepsilon_\alpha(q_\alpha\coth(q_\alpha)-1)\frac{\phi_3-\phi_1}{h_\alpha}+\varepsilon_\alpha h_\alpha\coth(q_\alpha)(q_\alpha\coth(q_\alpha)-1)\frac{\phi_1-2\phi_2+\phi_3}{h_\alpha^2}$$

Using these expressions sub-edge fluxes assume the forms

$$F_{12}(\boldsymbol{\phi}) = f_{12}+\varepsilon_\alpha h_\alpha(\coth(q_\alpha)-1)(q_\alpha\coth(q_\alpha)-1)\frac{\phi_1-2\phi_2+\phi_3}{h_\alpha^2},$$

and

$$F_{23}(\boldsymbol{\phi}) = f_{23}+\varepsilon_\alpha h_\alpha(\coth(q_\alpha)+1)(q_\alpha\coth(q_\alpha)-1)\frac{\phi_1-2\phi_2+\phi_3}{h_\alpha^2},$$

respectively. We can further rewrite sub-edge fluxes as

$$F_{12}(\boldsymbol{\phi}) = f_{12}+\frac{u_\alpha h_\alpha^2}{4}\Psi(-q_\alpha)\,\Delta_2(\boldsymbol{\phi}) \quad\text{and}\quad F_{23}(\boldsymbol{\phi}) = f_{23}+\frac{u_\alpha h_\alpha^2}{4}\Psi(q_\alpha)\,\Delta_2(\boldsymbol{\phi})$$

respectively, where

$$\Psi(x) = \frac{1}{x}(\coth(x)+1)(x\coth(x)-1)$$

is a monotonically increasing function taking values in $(0,2)$ and

$$\Delta_2(\boldsymbol{\phi}) = \frac{\phi_1-2\phi_2+\phi_3}{h_\alpha^2}$$

is central difference approximation of ϕ'' at segment midpoint $\boldsymbol{p}_2$. Combining these results yields

$$\begin{aligned}
F_h(\boldsymbol{\phi})|_{s_\alpha} &= \mathbf{i}\left(\left(f_{12}+\frac{u_\alpha h_\alpha^2}{4}\Psi(-q_\alpha)\Delta_2(\boldsymbol{\phi})\right)\left(\frac{3}{2}-\frac{2s}{h_\alpha}\right)+\left(f_{23}+\frac{u_\alpha h_\alpha^2}{4}\Psi(q_\alpha)\Delta_2(\boldsymbol{\phi})\right)\left(\frac{2s}{h_\alpha}-\frac{1}{2}\right)\right)\\
&= \mathbf{i}(\mathcal{I}(f_{12},f_{23};s)+\Theta(\boldsymbol{\phi},s)),
\end{aligned}$$

with

$$\mathcal{I}(f_{12}, f_{23}; s) = f_{12}\Big(\frac{3}{2} - \frac{2s}{h_\alpha}\Big) + f_{23}\Big(\frac{2s}{h_\alpha} - \frac{1}{2}\Big)$$

and

$$\Theta(\boldsymbol{\phi}, s) = \frac{u_\alpha h_\alpha^2}{4}\left(\Psi(-q_\alpha)\Delta_2(\boldsymbol{\phi})\Big(\frac{3}{2} - \frac{2s}{h_\alpha}\Big) + \Psi(q_\alpha)\Delta_2(\boldsymbol{\phi})\Big(\frac{2s}{h_\alpha} - \frac{1}{2}\Big)\right).$$

The first term is the linear interpolant of flux approximations f_{12} and f_{23} at sub-edge midpoints. We now focus attention on $\Theta(\boldsymbol{\phi}, s)$, which provides the stabilizing effect in the formulation.

To analyze this term, consider the Taylor expansions of $\phi'(s)$ about sub-edge midpoints

$$\phi'(s) = \phi'(\boldsymbol{m}_{12}) + \phi''(\boldsymbol{m}_{12})(s - h/4) + O(h_\alpha^2) \quad \text{and} \quad \phi'(s) = \phi'(\boldsymbol{m}_{23}) + \phi''(\boldsymbol{m}_{23})(s - 3h/4) + O(h_\alpha^2).$$

If the mesh is fine enough we can approximate second derivative values at sub-edge midpoints by the central difference $\Delta_2(\boldsymbol{\phi})$. Substituting this approximation in the above equations, solving for $\Delta_2(\boldsymbol{\phi})$ and multiplying the result by $2/h_\alpha$ yields

$$\Delta_2(\boldsymbol{\phi})\left(\frac{2s}{h_\alpha} - \frac{1}{2}\right) = \frac{2}{h_\alpha}\left(\phi'(s) - \phi'(\boldsymbol{m}_{12}) + O(h_\alpha^2)\right)$$

and

$$\Delta_2(\boldsymbol{\phi})\left(\frac{3}{2} - \frac{2s}{h_\alpha}\right) = \frac{2}{h}\left(\phi'(\boldsymbol{m}_{23}) - \phi'(s) + O(h_\alpha^2)\right).$$

Using these expressions and neglecting higher order terms we can write $\Theta(\boldsymbol{\phi}, s)$ as

$$\begin{aligned}\Theta(\boldsymbol{\phi}, s) &= \frac{u_\alpha h_\alpha}{2}\left(\Psi(-q_\alpha)\left(\phi'(\boldsymbol{m}_{23}) - \phi'(s)\right) + \Psi(q_\alpha)\left(\phi'(s) - \phi'(\boldsymbol{m}_{12})\right) + O(h_\alpha^2)\right)\\ &= \frac{u_\alpha h_\alpha}{2}\left(\phi'(s)(\Psi(q_\alpha) - \Psi(-q_\alpha)) + \Psi(-q_\alpha)\phi'(\boldsymbol{m}_{23}) - \Psi(q_\alpha)\phi'(\boldsymbol{m}_{12})\right)\end{aligned}$$

This formula is exact for quadratic functions. Taking into account that

$$\Psi(q_\alpha) - \Psi(-q_\alpha) = \frac{2}{q_\alpha}(q_\alpha \coth q_\alpha - 1)$$

yields the final expression for the stabilizing term along segment $\boldsymbol{s}_\alpha$:

$$\Theta(\boldsymbol{\phi}, s) = 4\varepsilon_\alpha \phi'(s)(q_\alpha \coth q_\alpha - 1) + [\Psi(-q_\alpha)\phi'(\boldsymbol{m}_{23}) - \Psi(q_\alpha)\phi'(\boldsymbol{m}_{12})]$$

The first term is a diffusive stabilizing flux. The difference in the square brackets is exponentially fitted approximation of the second derivative, i.e., it is an anti-diffusive term, which balances the amount of dissipation introduced by the first term and yields second-order accuracy.

4. Numerical studies

In this section we compare the multi-scale CVFEM (CVFEM-MS) with the classical streamline-upwind Petrov-Galerkin (SUPG) finite element method [7] and the control volume finite element method with *streamline upwinding* (CVFEM-SU) [25, 24]. The latter stabilizes

(5) by augmenting the nodal flux with a diffusive streamline flux motivated by SUPG weighting functions. The resulting stabilized flux

$$F_{SU}(\phi_h) = F(\phi_h) + \tau(\mathbf{u}\nabla \cdot (\mathbf{u}\phi_h)), \tag{21}$$

uses the same mesh-dependent stabilization parameter τ as SUPG.

The comparative study in this section employes the original definition [7] of τ on quadrilateral elements, which requires a notion of directional Péclet numbers. The latter are defined using segments $\boldsymbol{s}_\xi$ and $\boldsymbol{s}_\eta$ corresponding to the medians of the sub-elements $K_s \in \widetilde{K}_h(\Omega)$. Their lengths $h_\xi = |\boldsymbol{s}_\xi|$ and $h_\eta = |\boldsymbol{s}_\eta|$ are the characteristic dimensions of sub-element K_s. The directional Péclet numbers along the two segments are defined according to

$$P_\xi = \frac{u_\xi h_\xi}{2\varepsilon} \quad \text{and} \quad P_\eta = \frac{u_\eta h_\eta}{2\varepsilon},$$

respectively, where $u_\xi = \mathbf{u} \cdot \boldsymbol{t}_\xi$ and $u_\eta = \mathbf{u} \cdot \boldsymbol{t}_\eta$ are the tangential velocities along $\boldsymbol{s}_\xi$ and $\boldsymbol{s}_\eta$. Following [7] we set

$$\tau|_{K_s} = \frac{h_\xi u_\xi}{2|\mathbf{u}|^2}\left(\coth P_\xi - \frac{1}{P_\xi}\right) + \frac{h_\eta u_\eta}{2|\mathbf{u}|^2}\left(\coth P_\eta - \frac{1}{P_\eta}\right) \quad \forall K_s \in \widetilde{K}_h(\Omega). \tag{22}$$

For definitions and properties of this parameter in more general application and mesh contexts we refer to [18, 7, 16, 19] and the references therein.

Since the average $h_s = \left(h_\xi + h_\eta\right)/2$ is a representative measure of the element size, the formula

$$P_s = \frac{|\mathbf{u}|h_s}{2\varepsilon}$$

provides a notion of an elemental Péclet number. We use the largest such number as a measure for the degree of "advection domination" in a given test problem.

In all examples the computational domain $\Omega = [0,1]^2$. The domain boundary $\Gamma = \Gamma_B \cup \Gamma_T \cup \Gamma_L \cup \Gamma_R$, where Γ_B, Γ_T, Γ_L and Γ_R are the bottom, top, left and right sides of Ω, respectively, and $K_h(\Omega)$ is partition of Ω into quadrilateral elements. The corresponding sub-element mesh $\widetilde{K}_h(\Omega)$ is defined according to the procedure in Section 1.1. We remind that the multi-scale flux approximation in the new CVFEM formulation uses second-order Nedelec edge elements defined with respect to $K_h(\Omega)$. Approximation of the scalar ϕ by all three methods in our study is by nodal bilinear elements defined on the sub-element mesh $\widetilde{K}_h(\Omega)$. Before presenting the numerical results we briefly discuss the assembly of of the CVFEM-MS linear system.

4.1. Assembly of the CVFEM linear system

The multi-scale CVFEM (9) is equivalent to a a $p_0 \times p_0$ system of linear algebraic equations $A\boldsymbol{\phi}_0 = \boldsymbol{f}$ for the unknown coefficient vector $\boldsymbol{\phi}_0$. To explain the assembly of this matrix it is convenient to introduce the p-dimensional vector

$$\boldsymbol{\phi}_j = (0, \ldots, \phi_j, \ldots, 0),$$

where ϕ_j is the element of $\boldsymbol{\phi}$ corresponding to a point $\boldsymbol{p}_j \in P(\overline{\Omega})$. From (16) it is clear that the sub-edge fluxes are linear functions of the coefficient vector $\boldsymbol{\phi}$ and so,

$$F_h(\boldsymbol{\phi}) = \sum_{\boldsymbol{p}_j \in P(\Omega)} F_h(\boldsymbol{\phi}_j) + \sum_{\boldsymbol{p}_j \in P(\Gamma)} F_h(\boldsymbol{\phi}_j).$$

Since $\boldsymbol{\phi}_j = g(\boldsymbol{p}_j)$ for all $\boldsymbol{p}_j \in P(\Gamma)$ the second term is a known quantity, which we denote by $F_{h,g}$. This partitioning of the multi-scale flux implies that

$$A_{ij} = \int_{\partial C_i} F_h(\boldsymbol{\phi}_j) \cdot \boldsymbol{n}\, dS \quad \text{and} \quad \boldsymbol{f}_i = \int_{C_i} f dV - \int_{\partial C_i} F_{h,g} \cdot \boldsymbol{n}\, dS \quad \text{for} \quad \boldsymbol{p}_i, \boldsymbol{p}_j \in P(\Omega)\,. \tag{23}$$

Let us examine more closely the computation of A_{ij}. Recall that $K(C_i)$ is the set of all elements having a non-empty intersection with control volume C_i. As a result,

$$\int_{\partial C_i} F_h(\boldsymbol{\phi}_j) \cdot \boldsymbol{n}\, dS = \sum_{K_s \in K(C_i)} \int_{\partial C_i \cap K_s} F_h(\boldsymbol{\phi}_j) \cdot \boldsymbol{n}\, dS\,.$$

The integrals under the sum only require the elemental restriction $F_h|_{K_s}$ given by

$$F_h(\boldsymbol{\phi}_j)|_{K_s} = \sum_{\xi \in E(K_s)} F_\xi(\boldsymbol{\phi}_j) \vec{W}_{\xi,s}\,,$$

where $\vec{W}_{\xi,s} = \vec{W}_\xi|_{K_s}$ are the elemental restriction of the edge element basis functions. As a result,

$$A_{ij} = \sum_{K_s \in K(C_i)} \sum_{\xi \in E(K_s)} F_\xi(\boldsymbol{\phi}_j) \int_{\partial C_i \cap K_s} \vec{W}_{\xi,s} \cdot \boldsymbol{n}\, dS\,.$$

In other words, assembly of the CVFEM algebraic system can be completed without formally constructing a basis for the global edge element space $E_h(\Omega)$. Combined with the fact that F_h operates on *nodal* degrees of freedom this means that implementation of the multi-scale CVFEM does not require global edge data structures.

However, if a global edge data structure is available, one can precompute the coefficients of all sub-edge fluxes ahead of time and store them in an array indexed by sub-edge number, thereby improving the efficiency of the assembly process.

4.2. Convergence rates

We estimate the convergence rates of CVFEM-MS, CVFEM-SU and SUPG by combining the manufactured solution

$$\phi(\boldsymbol{x}) = \sin(2\pi x)^2 \sin(2\pi y)$$

with two different velocity fields and two different diffusivity values. Specifically, we pair the constant velocity field from (24) and the variable velocity field from (26) with $\varepsilon = 1 \times 10^{-3}$ and $\varepsilon = 1 \times 10^{-5}$. Substitution of the exact solution, the velocity field, and the diffusion coefficient into the PDE (1) defines the boundary data and the forcing term. The resulting four examples allow us to examine the behavior of the new method in a sufficiently representative range of operating conditions. Convergence rates are estimated by solving (1) on a sequence of uniform quadrilateral grids with $N \times N$ elements. Tables 1–2 summarize the results.

The data in these tables confirms numerically the second order accuracy of the new CVFEM-MS formulation. It also shows that the method performs consistently and robustly across all four test cases. In particular, convergence rates with constant and variable velocity fields are essentially the same. The observed orders of convergence are somewhat higher than expected in the more diffusive case. However, in the less diffusive case the L^2-norm and the H^1-seminorm errors match the theoretical best rates for bilinear elements.

Table 1: L^2-norm and H^1-seminorm errors on $N \times N$ uniform grids and the corresponding convergence rates of the multi-scale CVFEM (CVFEM-MS), the streamline-upwind CVFEM (CVFEM-SU) and the streamline-upwind Petrov-Galerkin finite element method (SUPG). The numbers in the parentheses give the size of the sub-element mesh. Constant velocity field (24).

Method		CVFEM-MS		CVFEM-SU		SUPG	
Error		L^2 error	H^1 error	L^2 error	H^1 error	L^2 error	H^1 error
N	max P_s	$\varepsilon = 1 \times 10^{-3}$					
16(32)	15.62	0.1128E-01	0.6921E+00	0.7628E-01	0.9576E+00	0.2974E-02	0.3894E+00
32(64)	7.81	0.2346E-02	0.3188E+00	0.3428E-01	0.4843E+00	0.7080E-03	0.1941E+00
64(128)	3.91	0.4395E-03	0.1331E+00	0.1352E-01	0.2264E+00	0.2014E-03	0.9703E-01
Rate		2.27	1.20	1.34	1.09	1.81	1.00
		$\varepsilon = 1 \times 10^{-5}$					
16(32)	1562.5	0.1357E-01	0.7600E+00	0.8535E-01	0.1075E+01	0.3047E-02	0.3912E+00
32(64)	781.25	0.3287E-02	0.3842E+00	0.4273E-01	0.6043E+00	0.6727E-03	0.1946E+00
64(128)	390.62	0.8054E-03	0.1927E+00	0.2130E-01	0.3569E+00	0.1589E-03	0.9714E-01
Rate		2.06	1.00	1.00	0.76	2.08	1.00

Table 2: L^2-norm and H^1-seminorm errors on $N \times N$ uniform grids and the corresponding convergence rates of the multi-scale CVFEM (CVFEM-MS), the streamline-upwind CVFEM (CVFEM-SU) and the streamline-upwind Petrov-Galerkin finite element method (SUPG). The numbers in the parentheses give the size of the sub-element mesh. Variable velocity field (26).

Method		CVFEM-MS		CVFEM-SU		SUPG	
Error		L^2 error	H^1 error	L^2 error	H^1 error	L^2 error	H^1 error
N	max P_s	$\varepsilon = 1 \times 10^{-3}$					
16(32)	30.83	0.6066E-02	0.6726E+00	0.4699E-01	0.7578E+00	0.1435E-02	0.3904E+00
32(64)	15.52	0.1267E-02	0.3137E+00	0.2148E-01	0.3534E+00	0.4489E-03	0.1943E+00
64(128)	7.78	0.2656E-03	0.1380E+00	0.8887E-02	0.1542E+00	0.1664E-03	0.9703E-01
Rate		2.28	1.16	1.27	1.19	1.43	1.00
		$\varepsilon = 1 \times 10^{-5}$					
16(32)	3083.2	0.7233E-02	0.7448E+00	0.5185E-01	0.8213E+00	0.1105E-02	0.3927E+00
32(64)	1552.1	0.1733E-02	0.3800E+00	0.2623E-01	0.4157E+00	0.1750E-03	0.1951E+00
64(128)	778.6	0.4250E-03	0.1911E+00	0.1313E-01	0.2082E+00	0.2912E-04	0.9726E-01
Rate		2.07	1.00	0.99	0.99	2.59	1.00

Results in Tables 1–2 confirm the first-order accuracy of the CVFEM-SU formulation. Solution errors and convergence rates of this method follow the same pattern as those of the CVFEM-MS., i.e., reducing ε reduces slightly the rates, but changing the velocity does not seem to affect them.

Finally, our results also reveal some inconsistency in the L^2-norm convergence rates of the SUPG. Somewhat counterintuitively, we see these rates *drop* for the more diffusive examples, whereas one would expect the opposite behavior. On the other hand, the H^1-seminorm errors of the SUPG are exceptionally robust and consistent in all four test cases.

4.3. Qualitative studies

This section uses several standard advection tests to complement the convergence study of (9) by a more qualitative examination of the new method. The test problems are defined by setting $f = 0$ and specifying an advective velocity field, a set of Dirichlet boundary conditions for (1), and a diffusion coefficient ε. The boundary conditions are selected in a manner that produces

Table 3: Violation of global solution bounds by CVFEM-MS, CVFEM-SU and SUPG solutions on a 64×64 (128×128 sub-elements) uniform grid. More diffusive case: $\varepsilon = 1 \times 10^{-3}$.

Method	Exact bounds		CVFEM-MS		CVFEM-SU		SUPG		Galerkin	
Example (max P_s)	min	max	min	max	min	max	min	max	min	max
1 (3.91)	0.0	1.0	0.000	1.001	0.000	1.090	0.000	1.101	0.000	2.042
2 (3.91)	0.0	1.0	-0.001	1.025	-0.001	1.025	-0.002	1.033	-0.001	1.915
3 (7.78)	0.0	1.0	0.000	1.000	0.000	1.000	0.000	1.000	0.000	1.000
Cumulative bound violation in %			2.7%		11.6%		13.6%		195%	

solution features such as internal and/or boundary layers. As before we consider a more diffusive and a less diffusive version of each example, corresponding to $\varepsilon = 1 \times 10^{-3}$ and $\varepsilon = 1 \times 10^{-5}$, respectively.

Example 1. The advective velocity and the boundary conditions are given by

$$\mathbf{u} = \begin{pmatrix} -\sin \pi/6 \\ \cos \pi/6 \end{pmatrix} \quad \text{and} \quad g = \begin{cases} 1 & \text{on } \Gamma_B \cup \Gamma_R \\ 0 & \text{on } \Gamma_T \cup \Gamma_L \end{cases}, \tag{24}$$

respectively. The solution of (1) develops exponential boundary layers at $\Gamma_T \cup \Gamma_L$; see [18].

Example 2:. This example combines the velocity field from Example 1 with the following boundary condition:

$$g = \begin{cases} 0 & \text{on } \Gamma_L \cup \Gamma_T \cup (\Gamma_B \cap \{x \leq 0.5\}) \\ 1 & \text{on } \Gamma_R \cup (\Gamma_B \cap \{x > 0.5\}) \end{cases}. \tag{25}$$

Discontinuity in the boundary data gives rise to an internal layer of width $O(\sqrt{\varepsilon})$. Near Γ_T the solution of (25) develops an exponential boundary layer to match the prescribed boundary data on Γ_T; see [10, Example 3.1.3, p.118].

Example 3:. The advective velocity and the boundary data are given by

$$\mathbf{u} = \begin{pmatrix} 2(2y-1)(1-(2x-1)^2) \\ -2(2x-1)(1-(2y-1)^2) \end{pmatrix} \quad \text{and} \quad g = \begin{cases} 1 & \text{on } \Gamma_R \\ 0 & \text{on } \Gamma_B \cup \Gamma_T \cup \Gamma_L \end{cases}, \tag{26}$$

respectively. This problem models temperature distribution in a cavity with a "hot" external wall (Γ_R) and is specialization of the *double-glazing* problem [10, Example 3.1.4, p.119] to the unit square. The discontinuities at the two corners of the hot wall create boundary layers near its corners.

Preservation of physical solution bounds. In many practical applications solutions of (1) represent concentrations of, e.g., electrons and holes as in drift-diffusion models, or certain ionic species as in simulations of protein channels. In such cases physically meaningful solution values vary between 0 and 1. Significant violation of these bounds in numerical solutions can lead to unphysical simulation results especially for coupled multiphysics problems where (1) provides inputs for other constituent components.

Table 4: Violation of global solution bounds by CVFEM-MS, CVFEM-SU and SUPG solutions on a 64×64 (128×128 sub-elements) uniform grid. Less diffusive case: $\varepsilon = 1 \times 10^{-5}$.

Method	Exact bounds		CVFEM-MS		CVFEM-SU		SUPG		Galerkin	
Example (max P_s)	min	max	min	max	min	max	min	max	min	max
1 (390.62)	0.0	1.0	0.000	1.003	0.000	1.237	0.000	1.257	-0.369	6.560
2 (390.62)	0.0	1.0	-0.051	1.085	-0.028	1.277	-0.046	1.254	-1.544	6.206
3 (778.60)	0.0	1.0	-0.003	1.000	-0.276	1.019	-0.213	1.040	-0.340	1.246
Cumulative bound violation in %			14.2%		83.7%		82.0%		1326.0%	

To compare and contrast violation of physical solution bounds by the new CVFEM-MS and CVFEM-SU and SUPG we solve Examples 1–3 on a 64×64 uniform mesh having 128×128 sub-elements. The values of the exact solutions in these examples range between 0 and 1. Since neither one of the three methods is formally monotone, the purpose of the study is to asses the relative severity of the bounds violation by each method. To this end we report the minimum and maximum values of the finite element solutions for each example as well as the cumulative violation of physical bounds in percent for all three examples. We compute the latter by summing up the absolute values of solution undershoots and overshoots for the three examples. The unstablized Galerkin method serves as a reference point for this study.

Table 3 presents the data for the more diffusive case $\varepsilon = 1 \times 10^{-3}$. The three stabilized methods clearly outperform the unstabilized Galerkin formulation, whose cumulative bounds violation is almost 200%. Interestingly enough, this violation is acquired in Examples 1 and 2, whereas for Example 3 the three stabilized methods and the unstabilized Galerkin perform equally well. The three stabilized methods also perform comparably well for Example 2. The most significant difference in their behavior is observed in Example 1 for which CVFEM-SU and SUPG violate solution bounds by approximately 10%, whereas the violation of these bounds by CVFEM-MS is just 0.1%. This example is also the principal contributor to the cumulative bound violations by CVFEM-SU and SUPG, which stand at 11.6% and 13.6%, respectively, compared with only 2.7% for the CVFEM-SU. The matching behavior of CVFEM-SU and SUPG is not surprising at all if one recalls that these two methods share a common stabilization mechanism and identical definitions of the stabilization parameter τ.

Table 4 summarizes results for the less diffusive case $\varepsilon = 1 \times 10^{-5}$. As it could be expected, in this more challenging setting the unstabilizied Galerkin method clearly fails with over 1300% of cumulative bounds violation. Compared to the more diffusive case the cumulative bounds violation in CVFEM-MS, CVFEM-SU and SUPG increases by a factor of 5.26, 7.22, and 6.03, respectively. We also note that violation of physical solution bounds in CVFEM-SU and SUPG solutions is now essentially equidistributed across the three examples with approximately 25% per example. In contrast, bounds violation in CVFEM-MS solutions follows the same pattern as in the more diffusive case. Specifically, its bulk occurs in Example 2 where it reaches 13.6%, whereas in examples 1 and 2 it is negligible at 0.3%.

Resolution of solution features. The results presented so far suggest that the new CVFEM-MS formulation handles boundary layers in an exceptionally robust manner yielding almost monotone solutions in both more and less diffusive settings. When the problem has an internal layer, in the less diffusive setting the solution develops larger overshoots and undershoots, but they still remain well below the overshoots and undershoots in CVFEM-SU and SUPG. To corroborate

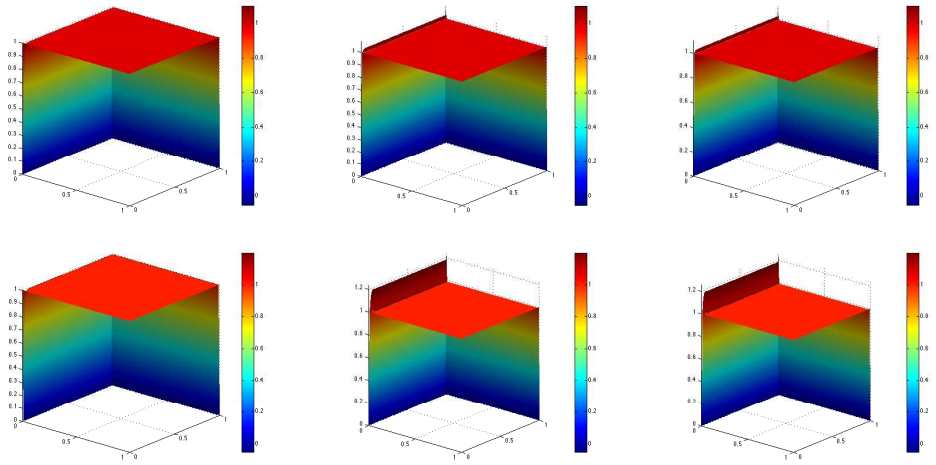

CVFEM-MS CVFEM-SU SUPG

Figure 5: Solution of Example 1 by CVFEM-MS, CVFEM-SU and SUPG on 64×64 mesh with 128×128 sub-elements. Top row: $\varepsilon = 1 \times 10^{-3}$. Bottom row: $\varepsilon = 1 \times 10^{-3}$.

these conclusions we present some plots of the CVFEM-MS, CVFEM-SU and SUPG solutions.

Figure 5 shows surface plots of the CVFEM-MS, CVFEM-SU and SUPG solutions of Example 1 for both values of the diffusion parameter ε. The figures clearly show the growth of the overshoot in the CVFEM-SU and SUPG solutions in the less diffusive case. The CVFEM-MS solution on the other hand continues to resolve this layer vert accurately

Figures 6–7 show surface and contour plots of the CVFEM-MS, CVFEM-SU and SUPG solutions of Example 2. In particular, Figure 7 suggest about the same level of smearing by all three methods. In the more diffusive case the three solutions are essentially identical in the 'eyeball norm", which is consistent with the data in Table 3. In the less diffusive case all three methods exhibit overshoots and undershoots along the internal layer caused by the discontinuity in the boundary data. However, their size in the CVFEM-MS remains about the same along the layer, whereas CVFEM-MS and SUPG develop significant overshoots exceeding 25% at the overflow boundary.

Finally, Figures 8–9 present surface and contour plots of CVFEM-MS, CVFEM-SU and SUPG solutions of Example 3. In the more diffusive case their solutions are once more virtually undistinguishable, suggesting that the three methods perform equally well. These conclusions are consistent with the data in Table 3, which shows no violation of physical solution bounds by the three methods. In the less-diffusive case CVFEM-MS exhibits 0.3% undershoot, which is too small to be seen in the figures. In contrast, CVFEM-SU and SUPG develop significant, visible undershoots along the right boundary.

5. Conclusions

We used $H(curl)$ lifting of multi-scale edge fluxes by second-order Nedelec edge elements to define a new, parameter-free stabilized control volume finite element method for advection-diffusion equations. Numerical studies of convergence rates using four different manufactured

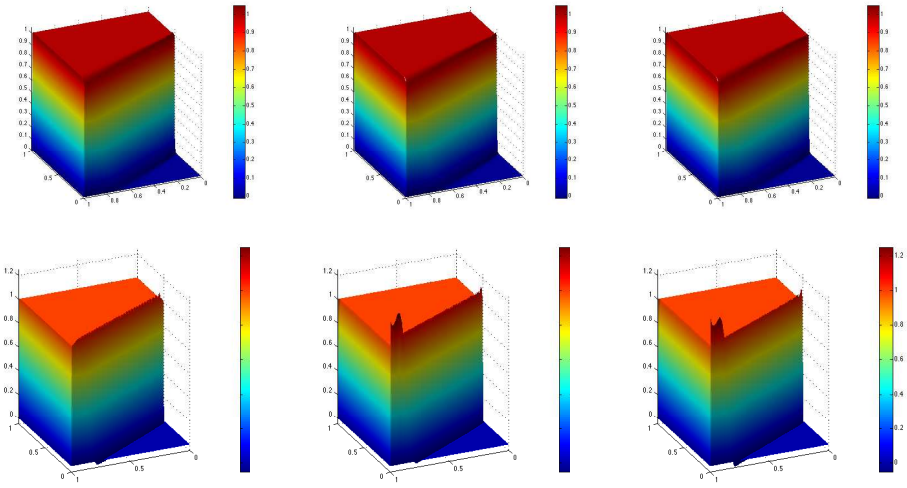

CVFEM-MS CVFEM-SU SUPG

Figure 6: Solution of Example 2 by CVFEM-MS, CVFEM-SU and SUPG on 64×64 mesh with 128×128 sub-elements. Top row: $\varepsilon = 1 \times 10^{-3}$. Bottom row: $\varepsilon = 1 \times 10^{-3}$.

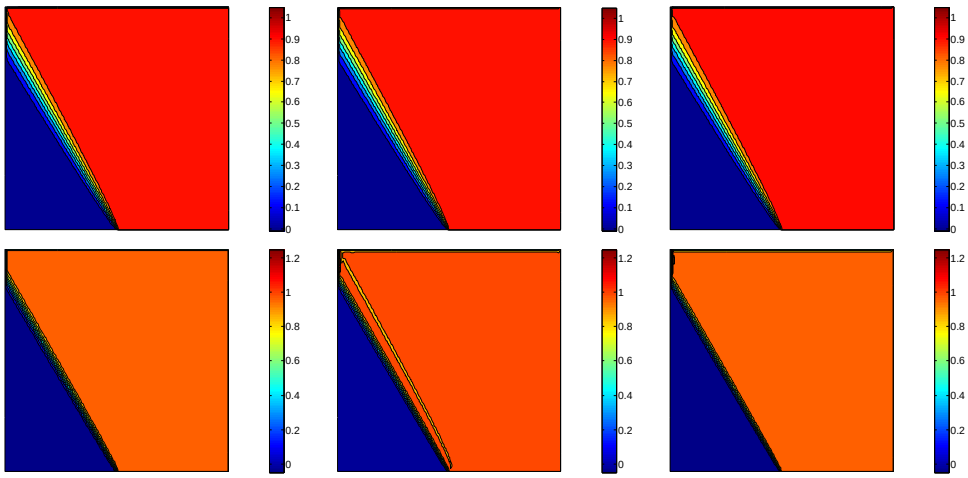

CVFEM-MS CVFEM-SU SUPG

Figure 7: Solution of Example 2 by CVFEM-MS, CVFEM-SU and SUPG on 64×64 mesh with 128×128 sub-elements. Top row: $\varepsilon = 1 \times 10^{-3}$. Bottom row: $\varepsilon = 1 \times 10^{-3}$.

solution configurations confirm that the new method is second-order accurate. Qualitative numerical studies of the method using standard advection tests reveal that the new formulation is exceptionally robust and accurate in resolving boundary layers. In particular, for problems having only boundary layers, the new method yields practically monotone solutions. Its ability to resolve internal layers caused by discontinuities in the boundary data is comparable to that of CVFEM-SU and SUPG and exhibits smaller overshoots and undershoots.

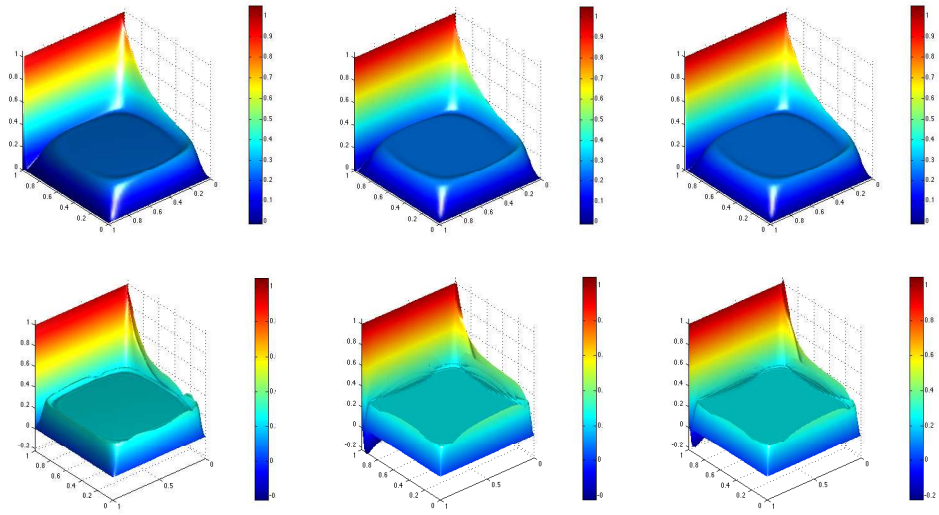

CVFEM-MS CVFEM-SU SUPG

Figure 8: Solution of Example 3 by CVFEM-MS, CVFEM-SU and SUPG on 64×64 mesh with 128×128 sub-elements. Top row: $\varepsilon = 1 \times 10^{-3}$. Bottom row: $\varepsilon = 1 \times 10^{-3}$.

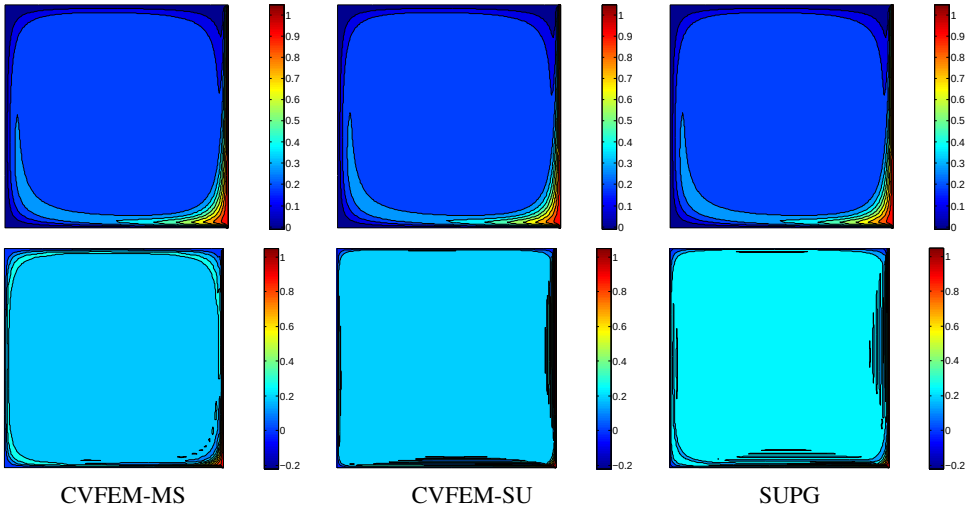

CVFEM-MS CVFEM-SU SUPG

Figure 9: Solution of Example 3 by CVFEM-MS, CVFEM-SU and SUPG on 64×64 mesh with 128×128 sub-elements. Top row: $\varepsilon = 1 \times 10^{-3}$. Bottom row: $\varepsilon = 1 \times 10^{-3}$.

Acknowledgment

The authors acknowledge funding by the DOE's Office of Science Advanced Scientific Computing Research Program (ASCR).

References

[1] Lutz Angermann and Song Wang. Three-dimensional exponentially fitted conforming tetrahedral finite elements for the semiconductor continuity equations. *Applied Numerical Mathematics*, 46(1):19 – 43, 2003.

[2] D. N. Arnold, R. S. Falk, and R. Winther. Finite element exterior calculus, homological techniques, and applications. *Acta Numerica*, 15:1–155, 2006.

[3] B.R. Baliga and S.V Patankar. New finite element formulation for convection-diffusion problems. *Numerical Heat Transfer*, 3(4):393–409, October 1980.

[4] P. Bochev, M. Perego, and K. Peterson. Formulation and analysis of a parameter-free stabilized finite element method. *SIAM J. Numer. Anal.*, Submitted., 2014.

[5] Pavel Bochev and Kara Peterson. A parameter-free stabilized finite element method for scalar advection-diffusion problems. *Central European Journal of Mathematics*, 11(8):1458–1477, 2013.

[6] Pavel Bochev, Kara Peterson, and Xujiao Gao. A new control volume finite element method for the stable and accurate solution of the drift–diffusion equations on general unstructured grids. *Computer Methods in Applied Mechanics and Engineering*, 254(0):126 – 145, 2013.

[7] Alexander N. Brooks and Thomas J.R. Hughes. Streamline upwind/Petrov-Galerkin formulations for convection dominated flows with particular emphasis on the incompressible Navier-Stokes equations. *Computer Methods in Applied Mechanics and Engineering*, 32(1–3):199 – 259, 1982.

[8] Ramon Codina. Comparison of some finite element methods for solving the diffusion-convection-reaction equation. *Computer Methods in Applied Mechanics and Engineering*, 156(1-4):185 – 210, 1998.

[9] L. Demkowicz, P. Monk, L. Vardapetyan, and W. Rachowicz. De Rham diagram for hp finite element spaces. *Computers & Mathematics with Applications*, 39(7-8):29 – 38, 2000.

[10] H. C. Elman, D. J. Silvester, and A. J. Wathen. *Finite Elements and Fast Iterative Solvers with Applications in Incompressible Fluid Dynamics*. Numerical Mathematics and Scientific Computation. Oxford University Press, 2005.

[11] L. Franca, A. Madureira, L. Tobiska, and F. Valentin. Convergence analysis of a multiscale finite element method for singularly perturbed problems. *Multiscale Modeling & Simulation*, 4(3):839–866, 2005.

[12] Leopoldo P. Franca, Alexandre L. Madureira, and Frederic Valentin. Towards multiscale functions: enriching finite element spaces with local but not bubble-like functions. *Computer Methods in Applied Mechanics and Engineering*, 194(27–29):3006 – 3021, 2005.

[13] I. Harari and T. J. R. Hughes. What are C and h?: Inequalities for the analysis and design of finite element methods. *Comput. Meth. Appl. Mech. Eng.*, 97:157–192, 1992.

[14] Thomas Y. Hou and Xiao-Hui Wu. A multiscale finite element method for elliptic problems in composite materials and porous media. *Journal of Computational Physics*, 134(1):169 – 189, 1997.

[15] Thomas J.R. Hughes, Michel Mallet, and Mizukami Akira. A new finite element formulation for computational fluid dynamics: II. beyond SUPG. *Computer Methods in Applied Mechanics and Engineering*, 54(3):341 – 355, 1986.

[16] Volker John and Ellen Schmeyer. Finite element methods for time-dependent convection-diffusion-reaction equations with small diffusion. *Computer Methods in Applied Mechanics and Engineering*, 198(3-4):475 – 494, 2008.

[17] Claes Johnson, Uno Nävert, and Juhani Pitkäranta. Finite element methods for linear hyperbolic problems. *Computer Methods in Applied Mechanics and Engineering*, 45(1–3):285 – 312, 1984.

[18] P. Knobloch. On the definition of the SUPG parameter. *ETNA*, 32:76–89, 2008.

[19] Paul T. Lin, John N. Shadid, Marzio Sala, Raymond S. Tuminaro, Gary L. Hennigan, and Robert J. Hoekstra. Performance of a parallel algebraic multilevel preconditioner for stabilized finite element semiconductor device modeling. *Journal of Computational Physics*, 228(17):6250 – 6267, 2009.

[20] J. C. Nédélec. Mixed finite elements in R^3. *Numerische Mathematik*, 35:315–341, 1980. 10.1007/BF01396415.

[21] J. C. Nédélec. A new family of mixed finite elements in R^3. *Numerische Mathematik*, 50:57–81, 1986. 10.1007/BF01389668.

[22] Riccardo Sacco. Exponentially fitted shape functions for advection-dominated flow problems in two dimensions. *Journal of Computational and Applied Mathematics*, 67(1):161 – 165, 1996.

[23] D.L. Scharfetter and H.K. Gummel. Large-signal analysis of a silicon Read diode oscillator. *Electron Devices, IEEE Transactions on*, 16(1):64 – 77, jan 1969.

[24] C. R. Swaminathan and V. R. Voller. Streamline upwind scheme for control-volume finite elements, Part I. Formulations. *Numerical Heat Transfer, Part B: Fundamentals*, 22(1):95–107, 1992.

[25] C. R. Swaminathan, V. R. Voller, and S. V. Patankar. A streamline upwind control volume finite element method for modeling fluid flow and heat transfer problems. *Finite Elements in Analysis and Design*, 13(2-3):169 – 184, 1993.

[26] Song Wang. A novel exponentially fitted triangular finite element method for an advection-diffusion problem with boundary layers. *Journal of Computational Physics*, 134(2):253 – 260, 1997.

Appendix A. Second-order Nedelec edge elements of the first-kind on quadrilaterals

This section provides additional details about the edge elements used to define the multi-scale flux approximation. Consider a reference quadrilateral $\hat{K} = [-1,1] \times [-1,1]$ with reference coordinates $(\hat{x}, \hat{y})$ and let $Q_{r,s}$ be the space of all polynomials on $\hat{K}$ whose degree in the $\hat{x}$ and $\hat{y}$ coordinate directions does not exceed r and s, respectively.

The r-th order reference edge element space of the first kind $E_r(\hat{K}) = Q_{r-1,r} \times Q_{r,r-1}$, i.e., it contains polynomial vector fields $\hat{V} = (\hat{v}_1, \hat{v}_2)$ such that $\hat{v}_1 \in Q_{r-1,r}$ and $\hat{v}_2 \in Q_{r,r-1}$; see [20]. Since $\dim Q_{r,s} = (r+1)(s+1)$ it follows that $\dim E_r(\hat{K}) = 2r(r+1)$. This space is optimized for the approximation of $H(curl)$ vector fields in the sense that it is p-th order accurate with respect to both the L^2 and $H(curl)$ norms.

The multi-scale flux approximation (8) employes the second-order Nedelec space $E_2(\hat{K}) = Q_{1,2} \times Q_{2,1}$ with dimension $\dim E_2(\hat{K}) = 12$. To define a basis set $\{\hat{W}_\alpha\}_\alpha$ for $E_2(\hat{K})$ one needs to choose a unisolvent set of degrees-of-freedom $\Lambda = \{\ell_\alpha(\mathbf{u})\}$, where ℓ_α are linear functionals acting on a vector field $\mathbf{u}$. A necessary condition for unisolvency is that $\dim \Lambda = \dim E_2(\hat{K}) = 12$. The set Λ must also allow the gluing of the elemental spaces in a way that ensures tangential continuity of the resulting piecewise polynomial vector fields. The latter is a basic prerequisite for curl-conforming finite element spaces.

Let $\{\hat{\boldsymbol{e}}_\alpha\}$ be the set of all reference sub-edges with unit tangents and midpoints $\hat{\boldsymbol{t}}_\alpha$ and $\hat{\boldsymbol{m}}_\alpha$, respectively. In this paper we use a set of *interpolatory* degrees of freedom given by

$$\ell_\alpha(\mathbf{u}) = \mathbf{u}(\hat{\boldsymbol{m}}_\alpha) \cdot \hat{\boldsymbol{t}}_\alpha \tag{A.1}$$

that is, Λ comprises the tangential components of $\mathbf{u}$ at the 12 sub-edge midpoints. Let

$$p_{s_0} = (s - s_0)$$

and $\mathbf{i} = (1,0)$, $\mathbf{j} = (0,1)$ be the versors of the reference coordinate system. Using the sub-edge numbering in Fig. 1, it is not hard to see that $\{\hat{W}_\alpha\}_\alpha$ contains a set of 6 "horizontal"

$$\begin{aligned}
\hat{W}_{15} &= -\,\mathbf{i}\,\frac{1}{2} p_{1/2}(x) p_0(y) p_1(y); & \hat{W}_{52} &= \mathbf{i}\,\frac{1}{2} p_{-1/2}(x) p_0(y) p_1(y) \\
\hat{W}_{89} &= \mathbf{i}\, p_{1/2}(x) p_{-1}(y) p_1(y); & \hat{W}_{96} &= -\,\mathbf{i}\, p_{-1/2}(x) p_{-1}(y) p_1(y) \\
\hat{W}_{47} &= -\,\mathbf{i}\,\frac{1}{2} p_{1/2}(x) p_{-1}(y) p_0(y); & \hat{W}_{73} &= \mathbf{i}\,\frac{1}{2} p_{-1/2}(x) p_{-1}(y) p_0(y)
\end{aligned} \tag{A.2}$$

and a set of 6 "vertical"

$$\begin{aligned}
\hat{W}_{18} &= -\,\mathbf{j}\,\frac{1}{2} p_{1/2}(y) p_0(x) p_1(x); & \hat{W}_{84} &= \mathbf{j}\,\frac{1}{2} p_{-1/2}(y) p_0(x) p_1(x) \\
\hat{W}_{59} &= \mathbf{j}\, p_{1/2}(y) p_{-1}(x) p_1(x); & \hat{W}_{97} &= -\,\mathbf{j}\, p_{-1/2}(y) p_{-1}(x) p_1(x) \\
\hat{W}_{26} &= -\,\mathbf{j}\,\frac{1}{2} p_{1/2}(y) p_{-1}(x) p_0(x); & \hat{W}_{63} &= \mathbf{j}\,\frac{1}{2} p_{-1/2}(y) p_{-1}(x) p_0(x)
\end{aligned} \tag{A.3}$$

basis functions. Contravariant transformation of the reference basis yields an elemental basis set on every $K_s \in K_h(\Omega)$. Specifically, let F_{K_s} be a map between $\hat{K}$ and a quadrilateral $K_s \in K_h(\Omega)$ with Jacobian $J_{K_s}(\boldsymbol{x})$. Then,

$$\vec{W}_{\alpha,s}(\boldsymbol{x}) = J_{K_s}^{-T}(\boldsymbol{x}) \cdot \hat{W}_\alpha(\boldsymbol{x})$$

The set Λ specified in (A.1) allows to combine the elemental basis functions into global basis functions $\vec{W}_\alpha(\boldsymbol{x})$ satisfying (2).

Remark 2. *An alternative choice of degrees-of-freedom, which formally requires less regularity, is to set*

$$\ell_\alpha(\mathbf{u}) = \int_{\hat{e}_\alpha} \mathbf{u} \cdot \hat{\boldsymbol{t}}_\alpha \, ds,$$

that is, Λ comprises the circulations of the vector field $\mathbf{u}$ along the 12 sub-edges of the reference element. It is straightforward to check that this choice yields the exact same reference basis functions (A.2)–(A.3).

Appendix B. Extensions to three-dimensions

Extension of the multi-scale CVFEM formulation to conforming partitions $K_h(\Omega)$ of a three-dimensional region Ω into isoparametric hexahedral elements is straightforward. The surfaces connecting medians of opposing sides subdivide an element $K_s \in K_h(\Omega)$ into 8 hexahedral sub-elements K_{s_i}. The total number of sub-edges on each element is 54 and they form 27 segments. We construct a pair of sub-edge fluxes on each segment following the procedure described in Section 2.2, i.e., we specify these fluxes according to (16). Then we use (8) in conjunction with second-order Nedelec elements of the first kind to expand sub-edge fluxes into an elemental multi-scale flux approximation.

The corresponding reference element space $E_2(\hat{K}) = Q_{1,2,2} \times Q_{2,1,2} \times Q_{2,2,1}$ has dimension 54, i.e., its size matches the number of sub-edges in the reference hexahedral. It is easy to see that (A.1) is a unisolvent set of degrees-of-freedom. The structure of the resulting basis set is very similar to that of the quadrilateral reference basis (A.2)–(A.3), except that there is a third set of "vertical" basis functions corresponding to sub-edges on segments aligned with the reference $\hat{z}$ coordinate.